ACS Energy LETTERS



http://pubs.acs.org/journal/aelccp
Letter

# Exploiting Mismatch Strain and the β–α Phase Transition for Microstructural Engineering in Thermoelectric $Ag_2Se$

Yu Liu,*,# Tobias Kleinhanns,# Maria Chiara Spadaro, Aziz Genç, Sharona Horta, Navita Jakhar, Tommaso Costanzo, Ewelina P. Dutkiewicz-Kopczynska, Jordi Arbiol, Min Hong, and Maria Ibáñez*

Cite This: ACS Energy Lett. 2026, 11, 5752–5762

Read Online

ACCESS | Metrics & More | Article Recommendations | Supporting Information

**ABSTRACT:** Silver selenide ($Ag_2Se$) is a promising near-room-temperature thermoelectric material, but its narrow stoichiometric window and β–α phase transition complicate reproducible microstructure control. Here, we present a mismatch-assisted microstructure engineering strategy in which $Ag_2Se$ particles are treated with polyanionic ZnSe complexes and consolidated through the β–α transition to introduce ZnSe nanoprecipitates, $Ag_2Se$/ZnSe interfaces, and local strain fields. The crystallographic mismatch between ZnSe and $Ag_2Se$, together with the $Zn^{2+}/Ag^+$ size difference, amplifies phase-transition-induced deformation and promotes high-density dislocations with periodic strain modulations. This defect architecture suppresses grain coarsening, removes excess Ag, limits Ag-interstitial formation, and reduces lattice thermal conductivity through lattice softening and multiscale phonon scattering. $Ag_2Se$–4%ZnSe nanocomposites achieve a peak $zT_{max}$ of 1.13 at 369 K and a $zT_{avg}$ of 1.08 from 300 to 380 K, demonstrating mismatch-driven defect engineering through the β–α phase transition as a route for optimizing $Ag_2Se$-based thermoelectrics.

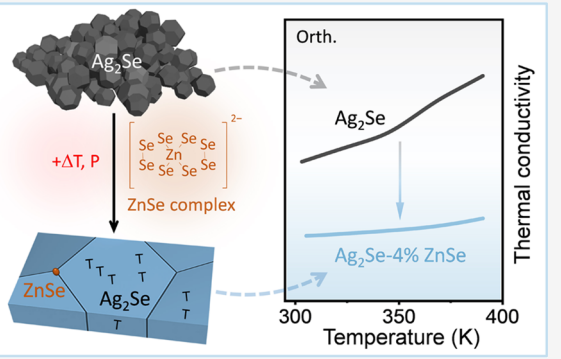


The growing demand for sustainable energy harvesting near room-temperature has increased interest in thermoelectric (TE) materials capable of converting low-grade waste heat from the human body, industrial processes, or ambient sources directly into electricity.[1−4] Among the most promising candidates for this temperature window is silver selenide ($Ag_2Se$), an intrinsically narrow-bandgap n-type semiconductor that combines high carrier mobility, glass-like lattice thermal conductivity ($\kappa_L$), and mechanical flexibility,[5−9] properties that are rare to find simultaneously in a single inorganic material. These characteristics place $Ag_2Se$ in a uniquely competitive position relative to the current near-room-temperature standard, $Bi_2Te_3$, which relies on scarce Te and is inherently brittle.[10−16]

Yet despite its appealing intrinsic properties, $Ag_2Se$ has proven difficult to optimize. First, the material has an exceptionally narrow homogeneity range, meaning that even small deviations from stoichiometry produce excess Ag precipitates or Se-rich defect clusters.[17] Excess Ag raises the carrier concentration well above the value required for maximum TE efficiency.[18] Minor Se excess has been shown to be beneficial by compensating Ag interstitials, but larger excess has been linked to poorly reproducible materials.[19] Second, a structural phase transition at ∼133 °C, where the room-temperature semiconducting orthorhombic phase (β-$Ag_2Se$) transforms into the superionic cubic phase (α-$Ag_2Se$) with dramatically different transport properties. This transition imposes a restriction on the temperature range over which high TE performance is achieved. Additionally, the phase transition generates large mechanical stresses due to the associated volume change, driving dislocation formation and microstructural rearrangement,[20,21] a source of complexity that is difficult to control reproducibly in conventional processing strategies. Therefore, a wide range of reported TE figures of merit is found in the literature,[6,17,22−25] indicating the sensitivity of these properties to processing.

Three broad strategies have been pursued to address these challenges. The first one focuses on microstructure engineering through processing alone, exploiting techniques such as spark plasma sintering,[20] cold sintering,[26−29] hot pressing,[30] and controlled synthesis of anisotropic nanostructures to tune grain size, porosity,[29,31] texture,[24,32,33] dislocation densities,[34,35] and the Ag/Se stoichiometric ratio during processing.[36] These processing-only approaches underscore how much microstructural leverage remains accessible in $Ag_2Se$ even before any chemical modification is introduced. The second strategy is chemical doping, in which aliovalent cations such as Cu,[37]

Received: May 15, 2026
Revised: June 29, 2026
Accepted: July 22, 2026
Published: August 3, 2026

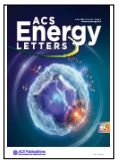

Pb,[38] Cd,[39] In,[22] or Sb,[40] are introduced to tune the carrier concentration and enhance phonon scattering via point defects. While effective in principle, doping in $Ag_2Se$ is constrained by the low solubility of foreign ions, which limits the achievable defect density and frequently forces excess dopants into forming secondary phases. The third strategy relies on nanocomposite engineering, embedding secondary-phase nanostructures within the $Ag_2Se$ matrix.[18,23,38,41,42] This approach has yielded meaningful reductions in $\kappa_L$, but the structural and chemical relationship between the secondary phase and the matrix, and in particular whether the elastic mismatch at that interface can be used as an active tool for defect engineering, has received little systematic attention.

Recent work has introduced another concept that the above strategies address only partially: the deliberate use of liquid–solid interfacial reactions during solution-phase processing to simultaneously correct off-stoichiometry, engineer grain boundary chemistry, and introduce secondary phases with controlled size and interfacial structure; all in a single low-temperature processing step.[18,43] The use of chalcogenidometallate complexes dissolved in the thiol-amine "alkahest" solvent system enables targeted reactions at particle surfaces that solid-state routes cannot replicate.[44−50] This principle was demonstrated with CdSe complexes, where interfacial reactions removed excess Ag and generated CdSe nanoprecipitates that reduced grain boundary mobility and suppressed $Ag^+$ diffusion, yielding a reproducible $zT$ of ∼1.04 across the full operating temperature range.

Herein, we extend this framework by using polyanionic ZnSe complexes to exploit the large mismatch that Zn introduces into the $Ag_2Se$ matrix. The origin of this mismatch is twofold. At the microstructural level, ZnSe nanoprecipitates adopt the cubic stilleite structure with lattice parameters significantly different from orthorhombic β-$Ag_2Se$, generating mismatch strain fields at the ZnSe/$Ag_2Se$ interfaces. At the atomic level, $Zn^{2+}$ (ionic radius ∼0.74 Å) is substantially smaller than $Ag^+$ (∼1.26 Å), meaning that any Zn that enters the $Ag_2Se$ matrix, whether transiently during sintering or as an interstitial atom, carries a large local elastic strain field. Critically, we exploit the phase transition itself to translate this strain landscape into a controlled defect architecture. During sintering, $Ag_2Se$ traverses the β–α phase transition, entering its superionic phase in which $Ag^+$ diffusivity increases by orders of magnitude and the large volume change drives significant mechanical deformation. We demonstrate that the coupling of interfacial mismatch strain and local lattice distortion with the β–α phase transition drives the formation of high-density periodic dislocation arrays evidenced by periodic strain modulations, which are only sparsely observed in untreated $Ag_2Se$ or when secondary-phase elements with smaller lattice mismatch are used, such as CdSe (ionic radius ∼0.96 Å). These high-density dislocation arrays suppress $\kappa_L$ through multiscale phonon-scattering and lattice softening while requiring significantly lower secondary-phase loadings, yielding a peak $zT_{max}$ of 1.13 at 369 K for $Ag_2Se$–4%ZnSe nanocomposites (NCPs).

## ■ ZNSE TREATMENT AND MISMATCH-STRAIN-ENGINEERED MICROSTRUCTURE

The introduction of Zn is done through interfacial reactions with $Ag_2Se$ using polyanionic ZnSe complexes prepared by dissolving stoichiometric amounts of ZnO and Se powder in a thiol-amine mixture at room temperature under a nitrogen atmosphere (Figure S1).[51] To understand the effects of the ZnSe treatment on the resulting materials, we first determine the chemical identity of the ZnSe complexes. High-resolution electrospray ionization mass spectrometry (HR-ESI-MS) identified $[ZnSe_8]^{2-}$ as the dominant species, with fragment ions $[Se_3]^-$ and $[ZnSe_n]^-$ ($n$ = 3–7) (Table S1), confirming their polyanionic character.[18] Surfactant-free $Ag_2Se$ particles, synthesized in aqueous solution and purified by successive centrifugation steps (Supporting Information, SI), are subsequently exposed to varying molar percentages ($x$ = 3, 4, and 5) of these complexes in *N*-methylformamide, followed by annealing at 400 °C and spark plasma sintering (SPS) at the same temperature (Figure 1a). These conditions expose the material to the $Ag_2Se$ β–α phase transition, which provides the mechanical deformation and high $Ag^+$ diffusivity conditions that determine the final microstructure. All pellets reach relative densities above 96% of their theoretical value (Table S2), and the compositions closely match the nominal ZnSe contents, as confirmed by inductively coupled plasma optical emission spectroscopy (ICP-OES) analysis (Table S3).

X-ray diffraction (XRD) patterns of all $Ag_2Se$–$x$%ZnSe pellets index exclusively to orthorhombic β-$Ag_2Se$, with no secondary phase reflections within detection limits and no shifts in peak positions across compositions (Figures 1b, S2, and S3). Rietveld refinement confirms that the lattice parameters remain unchanged regardless of the ZnSe content (Figures 1c and S4). Given the large size difference between $Zn^{2+}$ (∼0.74 Å) and $Ag^+$ (∼1.26 Å),[52] substitutional incorporation of Zn at Ag sites would produce a measurable lattice contraction. Conversely, previous work reports slight lattice expansion for Zn incorporation at very low concentrations in $Ag_2Se$, attributed to interstitial occupation.[25] The absence of either signature across all compositions confirms that Zn does not incorporate into the $Ag_2Se$ lattice in measurable quantities under our processing conditions. The large electronegativity difference between Ag (2.88) and Zn (2.26),[53] and the different crystal symmetry of $Ag_2Se$ and ZnSe, all thermodynamically disfavor solid solution formation. The quasi-binary $Ag_2Se$–ZnSe phase diagram corroborates immiscibility, showing that ZnSe solubility in $Ag_2Se$ is negligible and drops sharply below 545 °C (Figure 1d).[54] In situ heating XRD confirms that this picture holds across the full operating temperature range. Both untreated $Ag_2Se$ and the $Ag_2Se$–4%ZnSe NCP undergo a complete and reversible β–α phase transition at ca. 403 K, and their respective lattice parameters show normal thermal expansion but remain indistinguishable between the two compositions at all temperatures upon Rietveld refinement (Figures 1b,c, S5, and S6), confirming that Zn does not progressively dissolve into the $Ag_2Se$ lattice upon heating through the superionic phase.

Zn therefore resides primarily as ZnSe nanoprecipitates within the $Ag_2Se$ matrix, as confirmed by scanning transmission electron microscopy energy dispersive X-ray spectroscopy (STEM-EDX) elemental mapping (Figure 1e) and the high-resolution transmission electron microscopy (HRTEM) showing that these precipitates adopt the cubic stilleite structure ($F\bar{4}3m$, space group 216, Figure 1f), consistent with the negligible ZnSe solubility in $Ag_2Se$ predicted by the phase diagram and confirmed by structural refinement. Although the lattice parameters remain unchanged with varying ZnSe content, which indicates that Zn incorporation into the $Ag_2Se$ lattice is very limited and below laboratory XRD resolution, a trace amount of Zn-related point defects cannot be fully excluded.





https://doi.org/10.1021/acsenergylett.6c01499
ACS Energy Lett. 2026, 11, 5752−5762

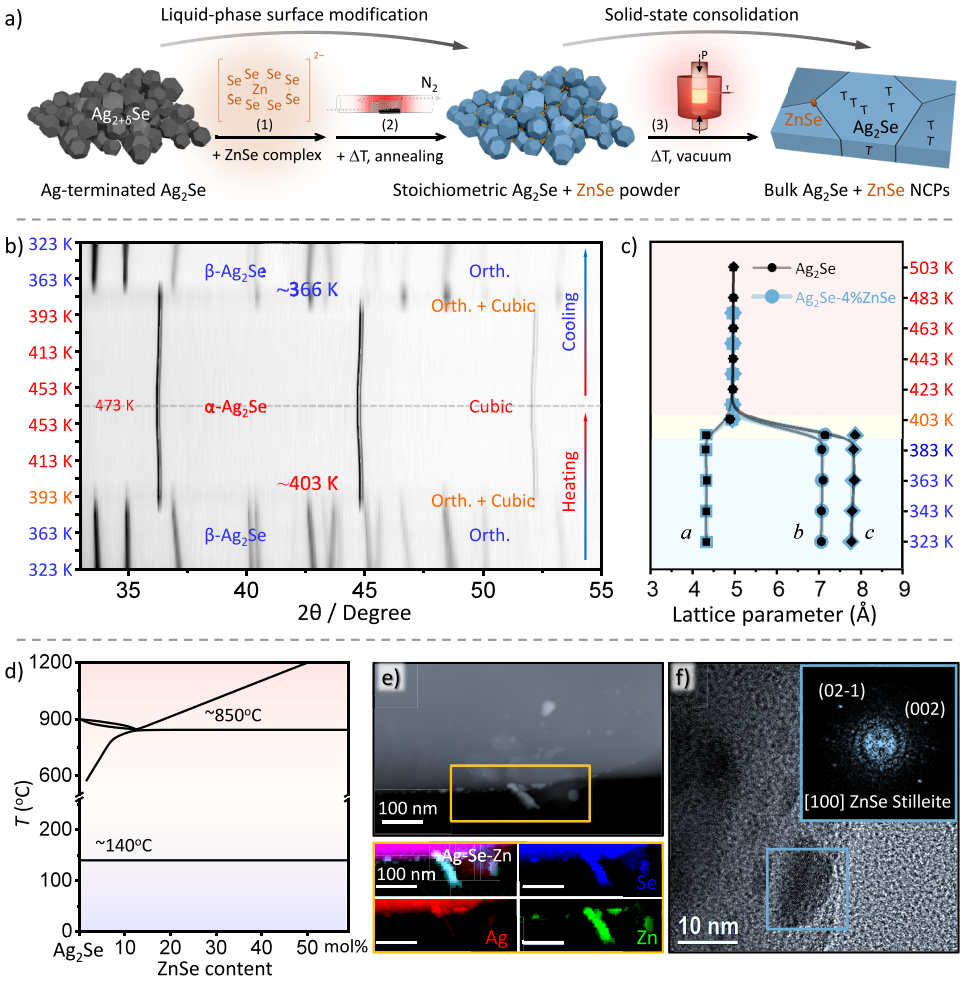


**Figure 1.** (a) Schematic illustration of the $Ag_2Se$–ZnSe NCPs preparation process: (1) surface modification of $Ag_2Se$ particles with polyanionic ZnSe complexes; (2) thermal annealing of the $Ag_2Se$–ZnSe powder composite under $N_2$; and (3) powder consolidation into dense pellets using SPS under vacuum. (b) HT-XRD of $Ag_2Se$–4%ZnSe pellet showing the 2D plot of intensity as functions of 2θ and temperature ($T$). (c) Corresponding lattice parameter comparison of untreated $Ag_2Se$ with $Ag_2Se$–4%ZnSe obtained from Rietveld refinement of the HT-XRD data. (d) Quasi-binary $Ag_2Se$–ZnSe phase diagram.[54] (e) ADF STEM image and corresponding EDX elemental maps of Ag (red), Se (blue), and Zn (green). (f) HRTEM image of a ZnSe nanoprecipitate embedded in the $Ag_2Se$ matrix, with the corresponding FFT pattern indexed to cubic stilleite ZnSe along the [100] zone axis.

The literature reports both ZnSe secondary phases and Zn interstitial doping in $Ag_2Se$, depending on concentration and processing route.[25,42] Moreover, the high $Ag^+$ diffusivity in the superionic phase has already been exploited to grow $Ag_2Se$/ZnSe heterostructures by supersaturation,[55] suggesting that limited Zn mobility into interstitial sites during the β–α phase transition is physically plausible at the low loadings used in this work.

The presence of ZnSe nanoprecipitates and any Zn-related point defects together creates a two-scale elastic strain landscape in the $Ag_2Se$ matrix: mismatch strain by the ZnSe/$Ag_2Se$ interfaces, and local strain fields from Zn point defects throughout the grain interior. Both contributions are activated or amplified by the β–α phase transition.[56,57] These independent bulk measurements directly confirm the development of this strain landscape. Williamson–Hall analysis shows microstrain increasing systematically with ZnSe content, directly confirming the development of mismatch-induced strain fields in the $Ag_2Se$ matrix (Figures 2a and S7). Sound velocity measurements reveal a 39% reduction in average sound velocity upon ZnSe incorporation (Figure 2b), directly evidencing lattice softening consistent with strain-induced reduction in effective elastic stiffness. Nanoindentation measurements show an approximately 42% increase in average hardness in $Ag_2Se$–4%ZnSe relative to untreated $Ag_2Se$ (Figures 2c and S8), reflecting the combined mechanical response to ZnSe inclusions and the strain-engineered defect microstructure. This strain landscape has two distinct and consequential effects on the microstructure: (i) it controls the grain size through impeding grain boundary migration, and (ii) it drives the formation of high-density dislocation arrays.

At the micrometer scale, thermal processing above the phase transition temperature drives significant grain coarsening in untreated $Ag_2Se$, a consequence of the liquid-like mobility of $Ag^+$ ions in the superionic phase that facilitates mass transport and grain coalescence (Figure 2d). ZnSe nanoprecipitates reduce grain boundary mobility, and progressively suppress grain coarsening with increasing ZnSe content, because $Ag_2Se$ and ZnSe do not form a solid solution across the operating temperature range. The electron backscatter diffraction (EBSD)



https://doi.org/10.1021/acsenergylett.6c01499
ACS Energy Lett. 2026, 11, 5752–5762

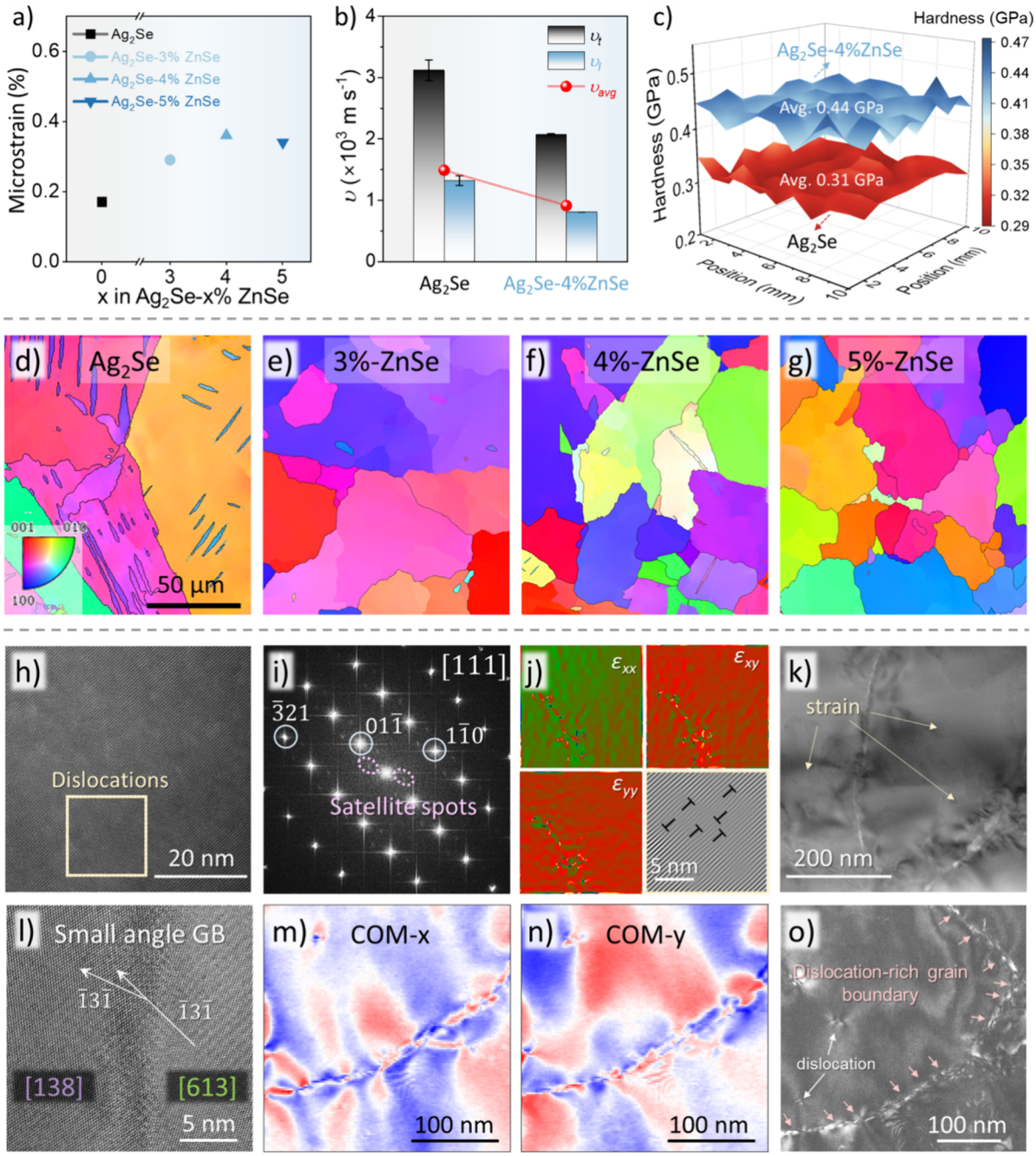


**Figure 2.** (a) Comparison of the Williamson–Hall derived microstrain for the different $Ag_2Se$–$x$%ZnSe ($x$ = 0, 3, 4, and 5) composites. (b) Room temperature transverse ($v_t$), longitudinal ($v_l$), and average ($v_{avg}$) acoustic sound velocities of untreated $Ag_2Se$ and $Ag_2Se$–4%ZnSe pellets. (c) 3D cloud hardness maps of untreated $Ag_2Se$, and $Ag_2Se$–4%ZnSe pellets. (d–g) EBSD orientation maps of untreated $Ag_2Se$ and $Ag_2Se$–$x$%ZnSe pellets with $x$ = 3, 4, and 5, respectively. (h) HRTEM image showing an inside grain region of the $Ag_2Se$–4%ZnSe NCPs. (i) Corresponding FFT pattern, with satellite spots (dotted circles). (j) IFFT image of the $01\bar{1}$ reflection, and dislocations observed in the yellow-squared region of (h), along with the corresponding GPA maps of the strain components $\varepsilon_{xx}$, $\varepsilon_{yy}$, and $\varepsilon_{xy}$. (k) Overview TEM image of highly strained and disordered microstructure. (l) HRTEM image of a small-angle grain boundary. (m) 4D-STEM based Center-of-Mass (COM) analysis showing local beam deflection maps in $x$-direction from strain fields and local electrostatic potential deviations, and (n) in $y$-direction. (o) WBDF image showing the dislocations at a grain boundary, and inside the grain as bright contrast.

orientation maps of $Ag_2Se$–$x$%ZnSe ($x$ = 0, 3, 4, and 5) pellets show this systematic reduction in grain size (Figure 2d–g). The stripe-like features observed within larger grains of untreated $Ag_2Se$ are consistent with deformation-induced lamellar features, likely including deformation twins, commonly observed in materials subjected to significant plastic deformation. It is reported that during the β–α phase transition, substantial plastic deformation takes place.[21] In ZnSe-treated samples, ZnSe precipitates and the increased grain boundary density both act as obstacles to dislocation motion and restrict the glide of partial dislocations required for twin nucleation and propagation, suppressing these lamellar features.



https://doi.org/10.1021/acsenergylett.6c01499
ACS Energy Lett. 2026, 11, 5752–5762

At the nanometer and atomic scales, TEM analysis of the $Ag_2Se$–4%ZnSe pellet reveals a microstructure qualitatively different from that of untreated $Ag_2Se$ in two aspects. First, the 10–50 nm Ag nanocrystals present in untreated $Ag_2Se$ and distributed throughout the matrix (Figure S9), are absent in the ZnSe-treated material (Figures 2h, S10, and S11). Their removal is attributed to the dissolution power of residual thiol-amine solvent from the ZnSe complex preparation, which is known to dissolve multiple bulk inorganic materials into reactive molecular species,[58−60] combined with the direct reaction of ZnSe complexes with excess Ag at the particle surface, a mechanism established for the chemically analogous CdSe system (Figure S12).[18] Second, the ZnSe-treated sample exhibits a markedly higher dislocation density than the untreated $Ag_2Se$, which is supported by the bulk scale properties (Figure 2a–c). HRTEM images acquired from intragranular regions show the orthorhombic $Ag_2Se$ structure with additional diffuse satellite reflections at approximately $^1/_6(\bar{3}21)$ in the FFT (Figure 2i). These reflections are present throughout the $Ag_2Se$–4%ZnSe sample (Figure S13). Inverse FFT (IFFT) images constructed from these satellite spots reveal strain modulations distributed across the grain interior, and GPA strain maps confirm discrete localized strain fields consistent with dislocation cores (Figures 2j and S13), collectively supporting the presence of high-density dislocation arrays with periodic character. The highly strained microstructure is further evidenced through a lower magnification TEM image (Figure 2k). While satellite reflections can in principle arise from grain overlap moiré, the uniform periodicity observed through the sample is more consistent with a periodic structural feature intrinsic to the $Ag_2Se$–4%ZnSe microstructure than with a projection artifact, which would produce orientation-dependent periodicities varying across the sample. This interpretation is supported by 4D-STEM analysis (Figures 2m,n and S14): a virtual dark-field image generated from the satellite diffraction intensity from the position averaged condensed beam electron diffraction (PACBED) pattern highlights the same grain boundary and grain interior dislocation structures observed in the corresponding bright-field image under two-beam conditions (Figure S15) and weak beam dark-field (WBDF) image (Figure 2o), indicating that the satellite diffraction intensity is spatially correlated with dislocations and their associated local lattice distortions.

The origin of the dislocation array lies in the interplay between the two-scale mismatch strain discussed above and the phase transition. The reversible β–α phase transition in $Ag_2Se$ induces giant mechanical deformation, analogous to plastic deformation in metals, that generates dislocations throughout the material.[21] Our prior work on solution-processed $Ag_2Se$ established that the dislocation density increases significantly when the sintering temperature exceeds the β–α phase transition temperature, directly confirming that traversal of the phase transition is responsible for dislocation generation in $Ag_2Se$.[20] Grain boundaries can act as preferential nucleation sites during the phase-transition-induced deformation,[61,62] with the dislocation spacing in the grain interior inheriting the periodicity set by the grain boundary geometry.[63] HRTEM of a low-angle grain boundary provides direct evidence for this nucleation mechanism (Figure 2l): the FFT of this region shows satellite spots from both adjacent grains at identical positions (Figure S16), indicating a shared structural periodicity at the boundary consistent with a periodic dislocation array whose spacing is determined by the crystallographic misorientation between the two grains. The structural and elastic mismatch between ZnSe nanoprecipitates and the $Ag_2Se$ matrix raises the local stress concentrations at the interfaces, amplifying dislocation nucleation at grain boundaries beyond what the phase transition alone produces.[64] Any Zn-related point defects throughout the grain interior may contribute additional local strain fields, providing a driving force for dislocation generation away from interfaces.[65] Center-of-mass (COM) analysis of the bright-field disk was used to map local beam deflections arising from strain fields in the vicinity of dislocation structures (Figures 2m,n). The pronounced beam deflections observed in the COM-$x$ and COM-$y$ maps, appearing as localized regions of enhanced contrast at dislocation sites, together with the more gradual variations reflecting extended strain fields across the dislocation-rich regions, provide quantitative spatial mapping of the strain landscape associated with the dislocation network. Together, these strain sources explain both the high overall dislocation density and the presence of dislocation-related features deep within grain interiors, well away from visible ZnSe precipitates. Both the systematic microstrain increase with ZnSe content (Williamson–Hall analysis, Figures 2a and S7) and the direct visualization of dislocations by WBDF imaging (Figure 2o) are consistent with this picture.

The combination of a high-diffusivity superionic phase and a strong mismatch driving force finds close analogy in other material systems where periodic dislocation arrays emerge from the coupling of solute strain fields and thermally activated diffusion. In PbTe/Ag composites, the low solubility and high diffusivity of Ag in PbTe lead to solute accumulation at dislocation arrays, producing strain modulations with ∼5 nm periodicity.[66] Similarly, in Mg–Nd–Mn alloys, periodically spaced misfit dislocations at tilt grain boundaries develop ordered interfacial structures when diffusion is enabled, driven by atomic size mismatch as the dominant factor.[63] In both cases, the periodicity of the resulting structure is inherited from the grain boundary geometry, consistent with what is proposed in this work. The absence of equivalent periodic dislocation arrays in $Ag_2Se$ treated with CdSe,[18] where the smaller lattice mismatch between CdSe and $Ag_2Se$ generates weaker interfacial strain fields and a lower driving force for dislocation nucleation, indicates that mismatch magnitude is one controlling design parameter.

## ■ TRANSPORT PROPERTIES

The microstructural features described above each have direct and distinguishable consequences for charge carrier and phonon transport. We discuss these transport properties in the temperature range from 300–390 K (Figures 3 and 4), within the β-$Ag_2Se$ phase, where the material exhibits its highest TE performance.[5,6,67,68] The transport data across the phase transition temperature up to 440 K can be found in Figure S17.

Untreated $Ag_2Se$ exhibits a higher $\sigma$ than most reported bulk $Ag_2Se$-based materials,[20,25,69−78] due to the presence of Ag nanoprecipitates and Ag interstitials that increase the Hall carrier concentration ($n_H = 1.3 \times 10^{19}$ cm$^{-3}$) above the value for optimal $zT$ (Figure 3a,c).[18,79] Liquid–solid interfacial reactions of the $Ag_2Se$ particles with polyanionic ZnSe complexes address this in two different ways. First, surface excess Ag is removed, preventing the formation of Ag nanoprecipitates during consolidation, similar to the behavior previously observed for CdSe complexes.[18] Second, the mismatch strain fields associated with $Ag_2Se$/ZnSe heterointerfaces and the periodic



https://doi.org/10.1021/acsenergylett.6c01499
ACS Energy Lett. 2026, 11, 5752−5762

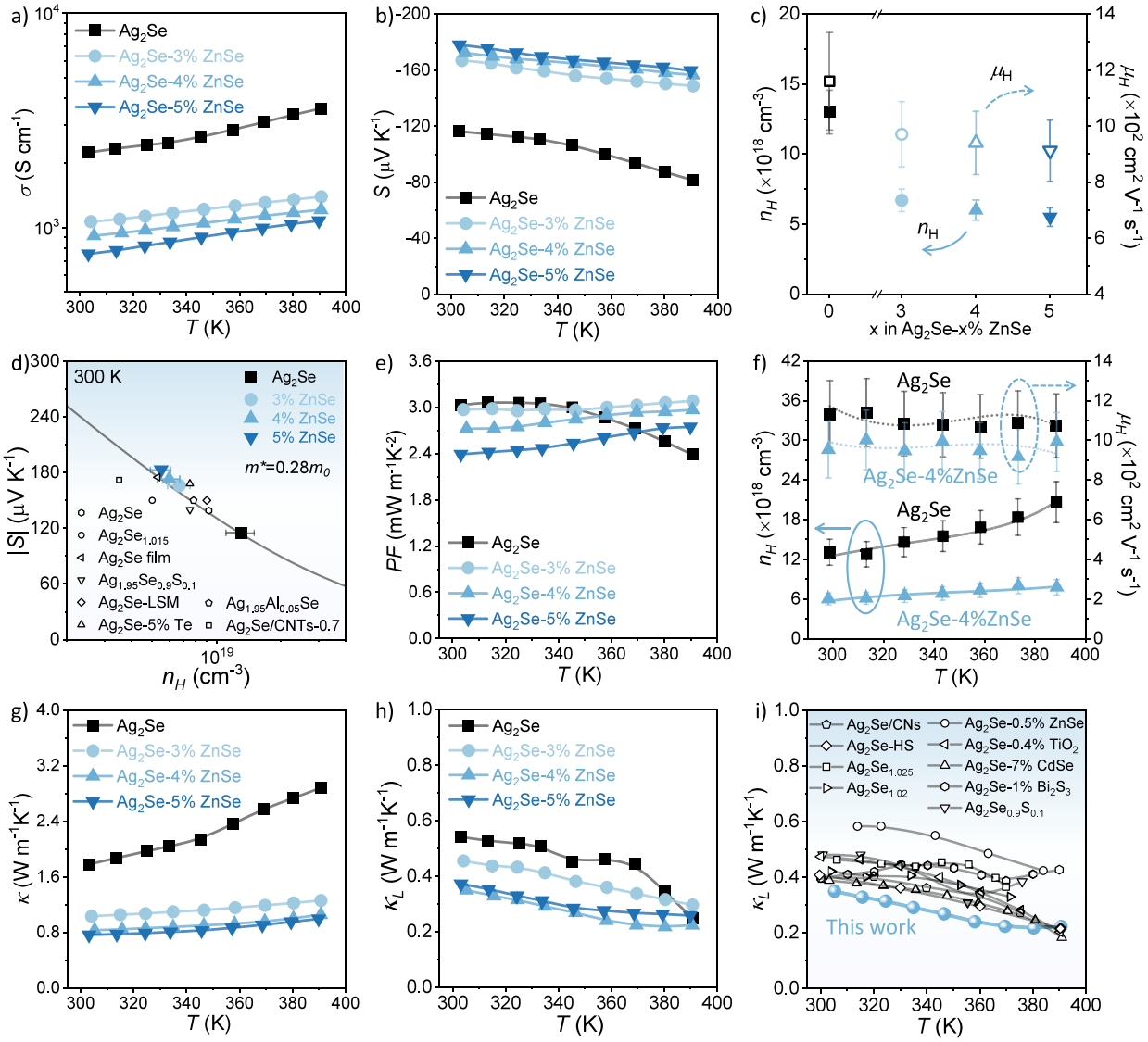


**Figure 3.** Transport properties of $Ag_2Se$–$x$%ZnSe ($x$ = 0, 3, 4, and 5) NCPs. Temperature dependence of (a) electric conductivity (σ) and (b) Seebeck coefficient ($S$). (c) Hall charge-carrier concentration ($n_H$, solid symbols) and carrier mobility ($\mu_H$, open symbols) at room temperature as a function of ZnSe content. (d) Pisarenko plot at 300 K. with black open dots representing reference data from other $Ag_2Se$-based TE materials.[69,73,76–78,81,82] (e) Temperature dependence of power factor (PF). (f) Temperature dependence of $n_H$ and $\mu_H$ for untreated $Ag_2Se$ and the $Ag_2Se$–4%ZnSe pellet. Temperature dependence of (g) thermal conductivity (κ), and (h) lattice thermal conductivity ($\kappa_L$). (i) Comparison of the temperature-dependent $\kappa_L$ values of $Ag_2Se$–4%ZnSe obtained in this work with those of previously reported $Ag_2Se$-based TE materials.[18,26,42,69,72,75,78,83,84]

dislocation arrays act as trapping sites for Ag interstitials,[42] suppressing their ionization[80] and hindering their formation with increasing temperature.[42] This is evidenced by the temperature-dependent $n_H$ measurements (Figure 3f). In untreated $Ag_2Se$, $n_H$ increases with temperature, reflecting the thermal activation of Ag atoms into interstitial sites while in the $Ag_2Se$–4%ZnSe NCP the increase is significantly smaller. Beyond the decrease in $n_H$, the Hall charge carrier mobility ($\mu_H$) of the $Ag_2Se$–ZnSe NCPs is progressively reduced as the Zn content increases, which is attributed to the increased density of interfaces that efficiently scatter charge carriers in $Ag_2Se$.[20]

The reduction of $n_H$ due to off-stoichiometry correction and interstitial trapping, together with the smaller $\mu_H$ caused by increased interface density, leads to an approximately threefold decrease of σ at room temperature from 2237 to 754 S cm$^{-1}$ (Figure 3a), and a corresponding increase in the absolute values of $S$, reaching −178 μV K$^{-1}$ for $Ag_2Se$–5%ZnSe at room temperature (Figure 3b). The unchanged effective mass ($m^* = 0.28m_0$) across all compositions, confirmed by the predicted Pisarenko relation (Figure 3d), indicates that these changes do not arise from ZnSe-induced band-structure modification. Overall, the NCPs achieve higher power factors ($PF = \sigma S^2$) at elevated temperatures, compared with the untreated $Ag_2Se$, as shown in Figure 3e.

The two-scale mismatch strain landscape that governs electronic transport also determines heat transport through the material. Compared with untreated $Ag_2Se$, all $Ag_2Se$–ZnSe NCPs





https://doi.org/10.1021/acsenergylett.6c01499
ACS Energy Lett. 2026, 11, 5752−5762

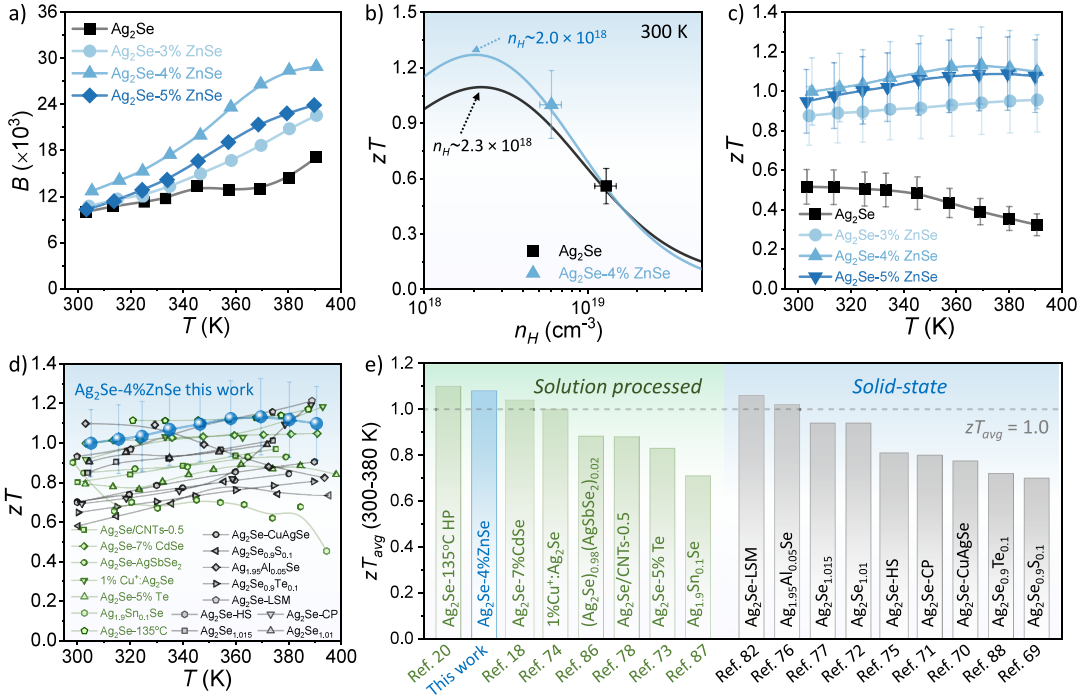


**Figure 4.** (a) Temperature dependence of quality factor ($B$). (b) $n_H$-dependent $zT$ values with both experimental data and predicted values for untreated $Ag_2Se$ and $Ag_2Se$–4%ZnSe at 300 K via calculations using the single parabolic band (SPB) model. The dashed arrows indicate the optimal $n_H$ for achieving peak $zT_{max}$ values. (c) Temperature dependence of TE figure of merit ($zT$) for $Ag_2Se$–$x$%ZnSe ($x$ = 0, 3, 4, and 5) NCPs. (d) Comparison of the temperature-dependent $zT$ values of $Ag_2Se$–4%ZnSe obtained in this work with those of previously reported state-of-the-art $Ag_2Se$-based TE materials, and (e) comparison of the average $zT_{avg}$ values of $Ag_2Se$–4%ZnSe NCPs with those of representative $Ag_2Se$-based TE materials produced by solution-processing methods[18,20,73,74,78,86,87] and solid-state methods[69−72,75−77,82,88] in the temperature range of 300–380 K.

exhibit significantly reduced κ (Figure 3g) and $\kappa_L$ (Figure 3h) values across the entire temperature range (Figure S18). For $Ag_2Se$–4%ZnSe NCPs, the room temperature κ and $\kappa_L$ are reduced by 50 and 35%, respectively, relative to untreated $Ag_2Se$. Notably, the $\kappa_L$ values of $Ag_2Se$–4%ZnSe are among the lowest reported for $Ag_2Se$-based TE materials in the near-room-temperature range (Figure 3i).[18,26,42,69,72,75,78,83,84] This reduction can be attributed to multiple phonon-scattering mechanisms operating over different length scales: (i) atomic scale mismatch strain fields from Zn point defects, (ii) extended periodic strain fields from dislocation arrays, and (iii) interface scattering from ZnSe nanoprecipitates. The synergistic contribution of these multiscale defects enables broadband phonon scattering, thereby effectively lowering $\kappa_L$.[85] In addition to these scattering mechanisms, a 39% reduction in average sound velocity upon ZnSe incorporation directly evidences lattice softening, which reduces phonon group velocity and contributes independently to $\kappa_L$ reduction (Figure 2b).

Although ZnSe treatment reduces $\mu_H$ through the increased grain boundary and interface density, the stronger reduction in $\kappa_L$ through multiscale phonon-scattering results in a net improvement of the TE quality factor ($B$) (Figure 4a).[89,90] Since $B$ is proportional to $\mu_W/\kappa_L$ (Figure S18d), its increase indicates that the reduction in $\kappa_L$ more than compensates for the mobility loss in the $Ag_2Se$–ZnSe NCPs. Carrier concentration analysis further shows that $Ag_2Se$–4%ZnSe shifts $n_H$ closer to the optimal range compared with untreated $Ag_2Se$ (Figure 4b). Consequently, all $Ag_2Se$–ZnSe NCPs exhibit enhanced $zT$ values, with $Ag_2Se$–4%ZnSe reaching a maximum $zT$ of 1.13 at 369 K (Figure 4c), which is superior to most other $Ag_2Se$-based TE materials prepared via solution-processed[18,20,73,74,78,86,87] and solid-state methods[69−72,75−77,82,88] (Figure 4d). More importantly, this enhanced performance extends across a broad temperature range, yielding a high average $zT$ value of ∼1.08 from ∼300 to 380 K (Figure 4e), with performance stability confirmed over repeated thermal cycling and sample-to-sample reproducibility verified by repeated measurements (Figures S19 and S20). To assess the practical potential of the material without the confounding variables of device fabrication, we calculated the theoretical conversion efficiency based on the measured transport properties. $Ag_2Se$–4%ZnSe achieves a theoretical efficiency of 4.4% under $\Delta T$ = 85 K, among the highest values reported for $Ag_2Se$-based TE materials across both solution-processed and solid-state routes (Figure S21), directly demonstrating the practical energy harvesting potential of the mismatch-driven defect engineering strategy.

In summary, we have shown that the β–α phase transition of $Ag_2Se$, combined with deliberately engineered mismatch strain, constitutes an effective microstructure design strategy. Treating $Ag_2Se$ particles with polyanionic ZnSe complexes and processing the resulting composite through the β–α phase transition drives the formation of a two-scale mismatch strain landscape and corrects stoichiometry through interfacial chemistry, suppresses Ag interstitial formation through strain-field trapping, and generates high-density dislocation arrays evidenced by periodic strain modulations that reduce $\kappa_L$ through multiscale phonon scattering and lattice softening more effectively than it



https://doi.org/10.1021/acsenergylett.6c01499
ACS Energy Lett. 2026, 11, 5752−5762

degrades carrier transport. Together, these effects lead to significantly enhanced $zT$ values, with the peak $zT$ increasing from 0.52 at room temperature for the untreated $Ag_2Se$ to 1.13 at 369 K for $Ag_2Se$–4%ZnSe NCPs. More importantly, this work demonstrates that mismatch magnitude and the kinetic conditions of the phase transition are critical design parameters, providing a design principle extendable to other phase-transitioning TE systems where solute mismatch and diffusivity can be similarly leveraged.

## ■ ASSOCIATED CONTENT

### Supporting Information

The Supporting Information is available free of charge at https://pubs.acs.org/doi/10.1021/acsenergylett.6c01499.

Details of additional materials characterization (X-ray diffraction patterns, SEM, TEM, extra electrical and thermal characterization), stability measurement, repeatability, and experimental procedures (PDF)

## ■ AUTHOR INFORMATION


### Corresponding Authors

**Yu Liu** – *Anhui Province Engineering Research Center of Flexible and Intelligent Materials, School of Chemistry and Chemical Engineering, Hefei University of Technology, Hefei 230009, China; Institute of Science and Technology Austria (ISTA), Am Campus 1, Klosterneuburg 3400, Austria;* orcid.org/0000-0001-7313-6740; Email: yliu@hfut.edu.cn

**Maria Ibáñez** – *Institute of Science and Technology Austria (ISTA), Am Campus 1, Klosterneuburg 3400, Austria;* orcid.org/0000-0001-5013-2843; Email: mibanez@ist.ac.at

### Authors

**Tobias Kleinhanns** – *Institute of Science and Technology Austria (ISTA), Am Campus 1, Klosterneuburg 3400, Austria*

**Maria Chiara Spadaro** – *Catalan Institute of Nanoscience and Nanotechnology (ICN2), CSIC and BIST, Campus UAB, Bellaterra, Barcelona, Catalonia 08193, Spain; Department of Physics and Astronomy "Ettore Majorana" and IMM-CNR, University of Catania, S. Sofia 64, Catania 95123, Italy*

**Aziz Genç** – *Catalan Institute of Nanoscience and Nanotechnology (ICN2), CSIC and BIST, Campus UAB, Bellaterra, Barcelona, Catalonia 08193, Spain*

**Sharona Horta** – *Institute of Science and Technology Austria (ISTA), Am Campus 1, Klosterneuburg 3400, Austria*

**Navita Jakhar** – *Institute of Science and Technology Austria (ISTA), Am Campus 1, Klosterneuburg 3400, Austria*

**Tommaso Costanzo** – *Institute of Science and Technology Austria (ISTA), Am Campus 1, Klosterneuburg 3400, Austria;* orcid.org/0000-0001-9732-3815

**Ewelina P. Dutkiewicz-Kopczynska** – *Institute of Science and Technology Austria (ISTA), Am Campus 1, Klosterneuburg 3400, Austria*

**Jordi Arbiol** – *Catalan Institute of Nanoscience and Nanotechnology (ICN2), CSIC and BIST, Campus UAB, Bellaterra, Barcelona, Catalonia 08193, Spain; ICREA, Pg, Lluís Companys 23, Barcelona, Catalonia 08010, Spain;* orcid.org/0000-0002-0695-1726

**Min Hong** – *Centre for Future Materials, School of Science, Engineering and Digital Technologies, University of Southern Queensland, Springfield Central, Queensland 4300, Australia;* orcid.org/0000-0002-6469-9194

Complete contact information is available at: https://pubs.acs.org/doi/10.1021/acsenergylett.6c01499


### Author Contributions

#Y.L. and T.K. contributed equally to this work. The manuscript was written with contributions from all authors. All authors have approved the final version of the manuscript.


### Funding Statement

Open access funding provided by Institute of Science and Technology Austria.


### Notes

The authors declare no competing financial interest.


## ■ ACKNOWLEDGEMENTS

M.I. acknowledges financial support from ISTA and the Werner Siemens Foundation. The Scientific Service Units (SSU) of ISTA supported this work through resources provided by the Electron Microscopy Facility (EMF), the Lab Support Facility (LSF), the Nanofabrication Facility (NNF), and the Mass Spectrometry Facility. Y.L. acknowledges funding from the National Natural Science Foundation of China (NSFC) (grant no. 22209034) and the Fundamental Research Funds for the Central Universities (JZ2024HGTB0239). M.H. acknowledges funding from Australian Research Council (FT230100316), and the high-performance computing resources provided by National Computational Infrastructure (it39) and Pawsey Supercomputing Centre (pawsey1075). ICN2 acknowledges funding from Generalitat de Catalunya 2021SGR00457. The authors thank support from the project AMaDE (PID2023-149158OB-C43), funded by MCIN/AEI/10.13039/501100011033/ and by the "ERDF Away of making Europe", by the "European Union". ICN2 is supported by the Severo Ochoa program from Spanish MCIN/AEI (grant no.: CEX2021-001214-S) and is funded by the CERCA Programme/Generalitat de Catalunya. Authors acknowledge the use of instrumentation as well as the technical advice provided by the Joint Electron Microscopy Center at ALBA (JEMCA). ICN2 acknowledges funding from Grant IU16-014206 (METCAM-FIB) funded by the European Union through the European Regional Development Fund (ERDF), with the support of the Ministry of Research and Universities, Generalitat de Catalunya. ICN2 is founding member of e-DREAM.[91]


## ■ REFERENCES


(1) Qin, B.; Kanatzidis, M. G.; Zhao, L. D. The Development and Impact of Tin Selenide on Thermoelectrics. *Science.* **2024,** *386* (6719), adp2444.

(2) Bell, L. E. Cooling, Heating, Generating Power, and Recovering Waste Heat with Thermoelectric Systems. *Science* **2008**, *321* (5895), 1457–1461.

(3) Ortega, S.; Ibáñez, M.; Liu, Y.; Zhang, Y.; Kovalenko, M. V.; Cadavid, D.; Cabot, A. Bottom-up Engineering of Thermoelectric Nanomaterials and Devices from Solution-Processed Nanoparticle Building Blocks. *Chem. Soc. Rev.* **2017**, *46* (12), 3510–3528.

(4) Liu, Y.; Ibáñez, M. Tidying up the Mess. *Science* **2021**, *371* (6530), 678–679.
(5) Wei, T.-R.; Qiu, P.; Zhao, K.; Shi, X.; Chen, L. $Ag_2Q$-Based (Q = S, Se, Te) Silver Chalcogenide Thermoelectric Materials. *Adv. Mater.* **2023**, *35* (1), 2110236.
(6) Wu, H.; Shi, X. L.; Duan, J.; Liu, Q.; Chen, Z. G. Advances in $Ag_2Se$-Based Thermoelectrics from Materials to Applications. *Energy Environ. Sci.* **2023**, *15* (5), 1870–1906.
(7) Lu, Y.; Qiu, Y.; Cai, K.; Ding, Y.; Wang, M.; Jiang, C.; Yao, Q.; Huang, C.; Chen, L.; He, J. Ultrahigh Power Factor and Flexible Silver Selenide-Based Composite Film for Thermoelectric Devices. *Energy Environ. Sci.* **2020**, *13* (4), 1240–1249.
(8) Jiang, F.; Lin, C.; Cheng, J.; Yu, H.; Zhou, Y.; Ma, X.; Wu, L.; Ye, S.; Chen, J.; Zhi, S.; Xu, Y.; Zhao, P.; Wang, X.; Cao, F.; Zhang, Q.; Mao, J. Prefer-Oriented $Ag_2Se$ Crystal for High-Performance Thermoelectric Cooling. *Adv. Funct. Mater.* **2025**, *35* (6), 2415000.
(9) Lyu, J.-M.; Zhang, L.; Yang, Y.-L.; Zhu, J.-F.; Shi, X.-L.; Chen, Z.-G. $Ag_2Se$-Based Thermoelectric Materials and Devices: Progress, Challenges, and Perspectives. *Energy Environ. Sci.* **2026**, *19* (10), 3134–3183.
(10) Zhu, T.; Hu, L.; Zhao, X.; He, J. New Insights into Intrinsic Point Defects in $V_2VI_3$ Thermoelectric Materials. *Adv. Sci.* **2016**, *3* (7), 1600004.
(11) Liu, Y.; Zhang, Y.; Lim, K. H.; Ibáñez, M.; Ortega, S.; Li, M.; David, J.; Martí-Sánchez, S.; Ng, K. M.; Arbiol, J.; Kovalenko, M. V.; Cadavid, D.; Cabot, A. High Thermoelectric Performance in Crystallographically Textured N-Type $Bi_2Te_{3-x}Se_x$ Produced from Asymmetric Colloidal Nanocrystals. *ACS Nano* **2018**, *12* (7), 7174–7184.
(12) Lu, Y.; Zhou, Y.; Wang, W.; Hu, M.; Huang, X.; Mao, D.; Huang, S.; Xie, L.; Lin, P.; Jiang, B.; Zhu, B.; Feng, J.; Shi, J.; Lou, Q.; Huang, Y.; Yang, J.; Li, J.; Li, G.; He, J. Staggered-Layer-Boosted Flexible $Bi_2Te_3$ Films with High Thermoelectric Performance. *Nat. Nanotechnol.* **2023**, *18* (11), 1281–1288.
(13) Zhang, Y.; Xing, C.; Liu, Y.; Li, M.; Xiao, K.; Guardia, P.; Lee, S.; Han, X.; Ostovari Moghaddam, A.; Josep Roa, J.; Arbiol, J.; Ibáñez, M.; Pan, K.; Prato, M.; Xie, Y.; Cabot, A. Influence of Copper Telluride Nanodomains on the Transport Properties of N-Type Bismuth Telluride. *Chem. Eng. J.* **2021**, *418*, 129374.
(14) Liu, Y.; Zhang, Y.; Ortega, S.; Ibáñez, M.; Lim, K. H.; Grau-Carbonell, A.; Martí-Sánchez, S.; Ng, K. M.; Arbiol, J.; Kovalenko V. M.; Cadavid, D.; Cabot, A. Crystallographically Textured Nanomaterials Produced from the Liquid Phase Sintering of $Bi_xSb_{2-x}Te_3$ Nanocrystal Building Blocks. *Nano Lett.* **2018**, *18* (4), 2557–2563.
(15) Tang, X.; Li, Z.; Liu, W.; Zhang, Q.; Uher, C. A Comprehensive Review on $Bi_2Te_3$-Based Thin Films: Thermoelectrics and Beyond. *Interdiscip. Mater.* **2022**, *1* (1), 88–115.
(16) Zhao, W.; Jin, K.; Xu, P.; Wu, F.; Fu, L.; Xu, B. Bismuth Telluride Supported Sub-1 Nm Polyoxometalate Cluster for High-Efficiency Thermoelectric Energy Conversion. *Nano Lett.* **2024**, *24* (17), 5361–5370.
(17) Huang, S.; Wei, T.-R.; Chen, H.; Xiao, J.; Zhu, M.; Zhao, K.; Shi, X. Thermoelectric $Ag_2Se$: Imperfection, Homogeneity, and Reproducibility. *ACS Appl. Mater. Interfaces* **2021**, *13* (50), 60192–60199.
(18) Liu, Y.; Kleinhanns, T.; Horta, S.; Dutkiewicz-Kopczynska, E. P.; Lu, S.; Spadaro, M. C.; Genç, A.; Chen, L.; Lim, K. H.; Hong, M.; Arbiol, J.; Ibáñez, M. Liquid–Solid Interface Reactions Drive Enhanced Thermoelectric Performance in $Ag_2Se$. *J. Am. Chem. Soc.* **2025**, *147* (35), 32199–32208.
(19) Mi, W.; Qiu, P.; Zhang, T.; Lv, Y.; Shi, X.; Chen, L. Thermoelectric Transport of Se-Rich $Ag_2Se$ in Normal Phases and Phase Transitions. *Appl. Phys. Lett.* **2014**, *104* (13), 133903.
(20) Kleinhanns, T.; Milillo, F.; Calcabrini, M.; Fiedler, C.; Horta, S.; Balazs, D.; Strumolo, M. J.; Hasler, R.; Llorca, J.; Tkadletz, M.; Brutchey, R. L.; Ibáñez, M. A Route to High Thermoelectric Performance: Solution-Based Control of Microstructure and Composition in $Ag_2Se$. *Adv. Energy Mater.* **2024**, *14* (22), 2400408.
(21) Liang, Q.; Yang, D.; Xia, F.; Bai, H.; Peng, H.; Yu, R.; Yan, Y.; He, D.; Cao, S.; Van Tendeloo, G.; Li, G.; Zhang, Q.; Tang, X.; Wu, J. Phase-Transformation-Induced Giant Deformation in Thermoelectric $Ag_2Se$ Semiconductor. *Adv. Funct. Mater.* **2021**, *31* (50), 2106938.
(22) Gou, Y.; Li, M.; Lyu, F.; Sun, X.; Huang, M.; Xie, W.; Hu, L.; Cao, W.; Hou, Y.; Liu, Y.; Cabot, A.; Wang, Z. Defect Driven Electronic Structure Reconfiguration and Hierarchical Phonon Suppression in $Ag_2Se$ Thermoelectrics. *Adv. Sci.* **2026**, e75408.
(23) Wang, H.; Liu, S.; Han, G.; Zhang, B.; Mo, X.; Chen, Y.; Zhang, K.; Lu, X.; Wang, G.; Zhou, X. Rational Design and Synthesis of Second Phases in N-Type $Ag_2Se$-Based Composites for Enhanced Thermoelectric and Mechanical Properties. *Acta Mater.* **2026**, *303*, 121728.
(24) Zhang, L.; Shi, X.-L.; Shang, H.; Gu, H.; Chen, W.; Li, M.; Huang, D.; Dong, H.; Wang, X.; Ding, F. High-Performance $Ag_2Se$-Based Thermoelectrics for Wearable Electronics. *Nat. Commun.* **2025**, *16* (1), 5002.
(25) Abusa, Y.; Yox, P.; Viswanathan, G.; Opare-Addo, J.; Sarkar, A.; Kyveryga, V.; Smith, E.; Lebedev, O. I.; Kovnir, K. A Recipe for a Great Meal: A Benchtop Route from Elemental Se to Superior Thermoelectric β-$Ag_2Se$. *J. Am. Chem. Soc.* **2024**, *146* (16), 11382–11391.
(26) Jakhar, N.; Kedia, D. K.; Kumar, A.; Saurabh, K.; Singh, S. Reproducible High Thermoelectric Figure of Merit in $Ag_2Se$. *Appl. Phys. Lett.* **2023**, *122* (16), 163901.
(27) Duangsimma, W.; Banlusan, K.; Pinitsoontorn, S. Cold Sintering Process with DMSO as a Transient Liquid for Efficient Improvement of Thermoelectric Properties in Silver Selenide. *Mater. Sci. Energy Technol.* **2025**, *8*, 154–165.
(28) Palaporn, D.; Pinitsoontorn, S.; Kurosaki, K.; Snyder, G. J. Porous $Ag_2Se$ Fabricated by a Modified Cold Sintering Process with the Average *ZT* around Unity near Room Temperature. *Adv. Mater. Technol.* **2024**, *9* (1), 2301242.
(29) Kitthonbancha, P.; Liu, W.; Li, M.; Pinitsoontorn, S.; Chen, Z. Transient Liquid Induced Hierarchical Structure Contributes to High Thermoelectric Performance in $Ag_2Se$. *Small* **2025**, *21* (11), 2411798.
(30) Santhosh, R.; Harish, S.; Abinaya, R.; Ponnusamy, S.; Ikeda, H.; Archana, J.; Navaneethan, M. Enhanced Thermoelectric Performance of Hot-Pressed N-Type $Ag_2Se$ Nanostructures by Controlling the Intrinsic Lattice Defects. *CrystEngComm* **2023**, *25* (22), 3317–3327.
(31) Xu, S.; Horta, S.; Lawal, A.; Maji, K.; Lorion, M.; Ibáñez, M. Interfacial Bonding Enhances Thermoelectric Cooling in 3D-Printed Materials. *Science* **2025**, *387* (6736), 845–850.
(32) Cao, T.; Shi, X.-L.; Hu, B.; Yang, Q.; Lyu, W.-Y.; Sun, S.; Yin, L.-C.; Liu, Q.-Y.; Chen, W.; Wang, X. Advancing $Ag_2Se$ Thin-Film Thermoelectrics via Selenization-Driven Anisotropy Control. *Nat. Commun.* **2025**, *16* (1), 1555.
(33) Xu, S.; Yang, S.; Qiu, P.; Gao, Z.; Gu, M.; Zheng, W.; Shi, X. Anisotropic Electrical Transports in Rolled $Ag_2Se$ Film. *Appl. Phys. Lett.* **2025**, *127* (22), 223903.
(34) Zhai, Q.; Zhu, B.; Gong, W.; Hou, Y.; Gu, R.; Pu, T.; Lei, C.; Liu, S.; Wang, Z.; Wang, D. Laser Shock Dislocation Proliferation Drives Enhanced Thermoelectric Performance in $Ag_2Se$. *Nano Lett.* **2025**, *25* (51), 17611–17618.
(35) Gao, Z.; Yang, S.; Ma, Y.; Wei, T.-R.; Chen, X.; Zheng, W.; Qiu, P.; Zeng, X.; Chen, L.; Shi, X. Warm Metalworking for Plastic Manufacturing in Brittle Semiconductors. *Nat. Mater.* **2025**, *24* (10), 1538–1544.
(36) Gao, J.; Li, J.; Miao, L.; Jia, L.; Qiu, P.; Yin, T.; Zhu, S.; Yang, X.; Guo, J.-C.; Chen, J.-L. Coherent Ag-Rich Nanoprecipitates/β-$Ag_2Se$ Flexible Film with Unprecedented Thermoelectric Performance by Liquid-like Sintering. *Nat. Commun.* **2025**, *16* (1), 6010.
(37) Liu, Y.; Wang, Z.; Li, J.; Zhang, M.; Liu, Y.; Han, X.; Zuo, X.; Cai, K.; Chen, L. Largely Enhanced Thermoelectric Performance of Flexible $Ag_2Se$ Film by Cationic Doping and Dual-Phase Engineering. *ACS Appl. Mater. Interfaces* **2024**, *16* (20), 26417–26427.
(38) Lim, K. H.; Xia, Y.; Xu, L.; Zhao, M.; Li, M.; Cheng, Y.; Mao, J.; Wang, S.; Chen, L.; Tsang, S. W.; Liu, P.; Wang, Q.; Yang, X.;




https://doi.org/10.1021/acsenergylett.6c01499
*ACS Energy Lett.* 2026, 11, 5752–5762

Wang, W.-J.; Cabot, A.; Hong, M.; Zhang, Y.; Liu, Y. Thermoelectric Performance in $Ag_2Se$ Nanocomposites: The Role of Interstitial Ag and Pb Orbital Hybridization. *Chem. Eng. J.* **2025**, *511*, 162265.
(39) Acharya, A.; Nagaraja, S.; Hassan, N.; Tarafder, K.; Ballav, N. High Thermoelectric Figure of Merit (ZT) in β-$Ag_2Se$ via Aliovalent Doping. *Small* **2025**, *21* (21), 2411498.
(40) Mathew, T.; Vijay, V.; Santhosh, R.; Senthilkumar, E.; Ponnusamy, S.; Navaneethan, M. Realization of Strain Field Origination via Sb Substitution in Naumannite $Ag_2Se$ for Room Temperature Power Generation. *J. Mater. Sci. Mater. Electron.* **2024**, *35* (19), 1321.
(41) Mo, Z.; Yang, M.; Li, H.; Zhang, M.; Zhu, H.; Zhou, Z.; Su, T. Optimizing Thermoelectric Performance of $Ag_2Se$ via $Sb_2Se_3$ Addition. *Vacuum* **2025**, *241*, 114613.
(42) Feng, B.; Cheng, Y.; Liu, C.; Gao, J.; Wu, G.; Bai, X.; Si, R.; Li, W.; Guo, Y.; Miao, L. Ag Interstitial Inhibition and Phonon Scattering at the ZnSe Nano-Precipitates to Enhance the Thermoelectric Performance of $Ag_2Se$. *ACS Appl. Energy Mater.* **2023**, *6* (5), 2804–2811.
(43) Ibáñez, M.; Boehme, S. C.; Buonsanti, R.; De Roo, J.; Milliron, D. J.; Ithurria, S.; Rogach, A. L.; Cabot, A.; Yarema, M.; Cossairt, B. M.; Reiss, P.; Talapin, D. V; Protesescu, L.; Hens, Z.; Infante, I.; Bodnarchuk, M. I.; Ye, X.; Wang, Y.; Zhang, H.; Lhuillier, E.; Klimov, V. I.; Utzat, H.; Rainò, G.; Kagan, C. R.; Cargnello, M.; Son, J. S.; Kovalenko, M. V. Prospects of Nanoscience with Nanocrystals: 2025 Edition. *ACS Nano* **2025**, *19* (36), 31969–32051.
(44) Ibañez, M.; Hasler, R.; Genc, A.; Liu, Y.; Kuster, B.; Schuster, M.; Dobrozhan, O.; Cadavid, D.; Arbiol, J.; Cabot, A.; Kovalenko, M. V. Ligand-Mediated Band Engineering in Bottom-up Assembled SnTe Nanocomposites for Thermoelectric Energy Conversion. *J. Am. Chem. Soc.* **2019**, *141* (20), 8025–8029.
(45) Ibáñez, M.; Genç, A.; Hasler, R.; Liu, Y.; Dobrozhan, O.; Nazarenko, O.; De La Mata, M.; Arbiol, J.; Cabot, A.; Kovalenko, M. V. Tuning Transport Properties in Thermoelectric Nanocomposites through Inorganic Ligands and Heterostructured Building Blocks. *ACS Nano* **2019**, *13* (6), 6572–6580.
(46) Chang, C.; Liu, Y.; Ho Lee, S.; Chiara Spadaro, M.; Koskela, K. M.; Kleinhanns, T.; Costanzo, T.; Arbiol, J.; Brutchey, R. L.; Ibáñez, M. Surface Functionalization of Surfactant-Free Particles: A Strategy to Tailor the Properties of Nanocomposites for Enhanced Thermoelectric Performance. *Angew. Chem., Int. Ed.* **2022**, *61* (35), e202207002.
(47) Shu, H.; Zhao, M.; Lu, S.; Wan, S.; Genç, A.; Huang, L.; Ibáñez, M.; Lim, K. H.; Hong, M.; Liu, Y. Influence of Surface Engineering on the Transport Properties of Lead Sulfide Nanomaterials. *J. Colloid Interface Sci.* **2025**, *683*, 703–712.
(48) Meng, W.; Xu, L.; Lu, S.; Li, M.; Li, M.; Zhang, Y.; Wang, Q.; Wang, W.-J.; Huo, S.; Bañares, M. A. Thiol–Amine Complexes for the Synthesis and Surface Engineering of SnTe Nanomaterials toward High Thermoelectric Performance. *ACS Nano* **2025**, *19* (38), 34395–34407.
(49) Strumolo, M. J.; Chen, Y.; Brutchey, R. L. Solution Processed CuAgS Absorber Layers from a Thiol-Amine-Based Ink. *J. Solid State Chem.* **2026**, *353*, 125664.
(50) McCarthy, C. L.; Downes, C. A.; Schueller, E. C.; Abuyen, K.; Brutchey, R. L. Method for the Solution Deposition of Phase-Pure $CoSe_2$ as an Efficient Hydrogen Evolution Reaction Electrocatalyst. *ACS Energy Lett.* **2016**, *1* (3), 607–611.
(51) McCarthy, C. L.; Webber, D. H.; Schueller, E. C.; Brutchey, R. L. Solution-Phase Conversion of Bulk Metal Oxides to Metal Chalcogenides Using a Simple Thiol-Amine Solvent Mixture. *Angew. Chem. Int. Ed.* **2015**, *54* (29), 8378–8381.
(52) Shannon, R. D. Revised Effective Ionic Radii and Systematic Studies of Interatomic Distances in Halides and Chalcogenides. *Acta Crystallogr. Sect. A* **1976**, *32* (5), 751–767.
(53) Tantardini, C.; Oganov, A. R. Thermochemical Electronegativities of the Elements. *Nat. Commun.* **2021**, *12* (1), 2087.
(54) Tomashyk, V.; Feychuk, P.; Shcherbak, L. *Ternary Alloys Based on II-VI Semiconductor Compounds*; CRC Press: Boca Raton London New York, **2013**.
(55) Zhou, J.; Huang, F.; Xu, J.; Wang, Y. Controllable Synthesis of Metal Selenide Heterostructures Mediated by $Ag_2Se$ Nanocrystals Acting as Catalysts. *Nanoscale* **2013**, *5* (20), 9714–9719.
(56) Ding, Z.; Li, P.; Qin, Z.; Huang, W.; Zhao, P.; Zhou, D.; Meng, X.; Sato, Y. S.; Dong, H. Strain-Mediated Defect Engineering toward Rapid Atomic Migration in Fe–Al Diffusion Couples. *Nano Lett.* **2024**, *24* (39), 12171–12178.
(57) Wu, Z.; You, Y.; Zhang, F.; Lü, T.-Y.; Cao, X.; Sun, Y.; Zhu, Z.-Z.; Wu, S. Elastic Softening and Defect-Mediated Diffusion in Superionic $Li_2O$ Revealed by Molecular Dynamics. *Phys. Rev. B* **2025**, *112* (18), 184106.
(58) Webber, D. H.; Buckley, J. J.; Antunez, P. D.; Brutchey, R. L. Facile Dissolution of Selenium and Tellurium in a Thiol-Amine Solvent Mixture under Ambient Conditions. *Chem. Sci.* **2014**, *5* (6), 2498–2502.
(59) McCarthy, C. L.; Brutchey, R. L. Solution Processing of Chalcogenide Materials Using Thiol–Amine "Alkahest" Solvent Systems. *Chem. Commun.* **2017**, *53* (36), 4888–4902.
(60) Zhao, X.; Deshmukh, S. D.; Rokke, D. J.; Zhang, G.; Wu, Z.; Miller, J. T.; Agrawal, R. Investigating Chemistry of Metal Dissolution in Amine–Thiol Mixtures and Exploiting It toward Benign Ink Formulation for Metal Chalcogenide Thin Films. *Chem. Mater.* **2019**, *31* (15), 5674–5682.
(61) Yamakov, V.; Wolf, D.; Phillpot, S. R.; Mukherjee, A. K.; Gleiter, H. Dislocation Processes in the Deformation of Nanocrystalline Aluminium by Molecular-Dynamics Simulation. *Nat. Mater.* **2002**, *1* (1), 45–49.
(62) Murr, L. E. Dislocation Ledge Sources: Dispelling the Myth of Frank–Read Source Importance. *Metall. Mater. Trans. A* **2016**, *47* (12), 5811–5826.
(63) Xie, H.; Huang, Q.; Bai, J.; Li, S.; Liu, Y.; Feng, J.; Yang, Y.; Pan, H.; Li, H.; Ren, Y.; Qin, G. Nonsymmetrical Segregation of Solutes in Periodic Misfit Dislocations Separated Tilt Grain Boundaries. *Nano Lett.* **2021**, *21* (7), 2870–2875.
(64) Peng, S.; Wei, Y.; Gao, H. Nanoscale Precipitates as Sustainable Dislocation Sources for Enhanced Ductility and High Strength. *Proc. Natl. Acad. Sci. U. S. A.* **2020**, *117* (10), 5204–5209.
(65) Wang, P.; Song, Z.; Li, Q.; Wang, H. Atomistic Simulation for the Interaction between Dislocation and Solute Atoms, Clusters, and Associated Physical Insights. *J. Appl. Phys.* **2020**, *128* (2), 24301.
(66) Yu, Y.; Zhang, S.; Mio, A. M.; Gault, B.; Sheskin, A.; Scheu, C.; Raabe, D.; Zu, F.; Wuttig, M.; Amouyal, Y.; Cojocaru-Mirédin, O. Ag-Segregation to Dislocations in PbTe-Based Thermoelectric Materials. *ACS Appl. Mater. Interfaces* **2018**, *10* (4), 3609–3615.
(67) Day, T.; Drymiotis, F.; Zhang, T.; Rhodes, D.; Shi, X.; Chen, L.; Snyder, G. J. Evaluating the Potential for High Thermoelectric Efficiency of Silver Selenide. *J. Mater. Chem. C* **2013**, *1* (45), 7568–7573.
(68) Zhao, K.; Qiu, P.; Shi, X.; Chen, L. Recent Advances in Liquid-Like Thermoelectric Materials. *Adv. Funct. Mater.* **2020**, *30* (8), 1903867.
(69) Liang, J.; Qiu, P.; Zhu, Y.; Huang, H.; Gao, Z.; Zhang, Z.; Shi, X.; Chen, L. Crystalline Structure-Dependent Mechanical and Thermoelectric Performance in $Ag_2Se_{1-x}S_x$ System. *Research* **2020**, *2020*, 6591981.
(70) Chen, J.; Sun, Q.; Bao, D.; Tian, B.-Z.; Wang, Z.; Tang, J.; Zhou, D.; Yang, L.; Chen, Z.-G. Simultaneously Enhanced Strength and Plasticity of $Ag_2Se$-Based Thermoelectric Materials Endowed by Nano-Twinned CuAgSe Secondary Phase. *Acta Mater.* **2021**, *220*, 117335.
(71) Yang, D.; Su, X.; Meng, F.; Wang, S.; Yan, Y.; Yang, J.; He, J.; Zhang, Q.; Uher, C.; Kanatzidis, M. G. Facile Room Temperature Solventless Synthesis of High Thermoelectric Performance $Ag_2Se$ via a Dissociative Adsorption Reaction. *J. Mater. Chem. A* **2017**, *5* (44), 23243–23251.





https://doi.org/10.1021/acsenergylett.6c01499
*ACS Energy Lett.* 2026, 11, 5752–5762

(72) Jood, P.; Chetty, R.; Ohta, M. Structural Stability Enables High Thermoelectric Performance in Room Temperature $Ag_2Se$. *J. Mater. Chem. A* **2020**, *8* (26), 13024–13037.
(73) Lim, K. H.; Wong, K. W.; Liu, Y.; Zhang, Y.; Cadavid, D.; Cabot, A.; Ng, K. M. Critical Role of Nanoinclusions in Silver Selenide Nanocomposites as a Promising Room Temperature Thermoelectric Material. *J. Mater. Chem. C* **2019**, *7* (9), 2646–2652.
(74) Tee, S. Y.; Tan, X. Y.; Wang, X.; Lee, C. J. J.; Win, K. Y.; Ni, X. P.; Teo, S. L.; Seng, D. H. L.; Tanaka, Y.; Han, M.-Y. Aqueous Synthesis, Doping, and Processing of N-Type $Ag_2Se$ for High Thermoelectric Performance at near-Room-Temperature. *Inorg. Chem.* **2022**, *61* (17), 6451–6458.
(75) Chen, J.; Sun, Q.; Bao, D.; Liu, T.; Liu, W.-D.; Liu, C.; Tang, J.; Zhou, D.; Yang, L.; Chen, Z.-G. Hierarchical Structures Advance Thermoelectric Properties of Porous N-Type β-$Ag_2Se$. *ACS Appl. Mater. Interfaces* **2020**, *12* (46), 51523–51529.
(76) Ahmad, S.; Sarkar, P.; Bhatt, P.; Bhattacharya, S.; Navaneethan, M.; Basu, R.; Bhatt, R.; Bohra, A.; Debnath, A. K.; Muthe, K. P. Improved Thermoelectric Performance of $Ag_{2-x}Al_xSe$ through Formation of AgAl Phase. *Appl. Phys. Lett.* **2022**, *121* (17), 173905.
(77) Wang, P.; Chen, J.-L.; Zhou, Q.; Liao, Y. T.; Peng, Y.; Liang, J. S.; Miao, L. Enhancing the Thermoelectric Performance of $Ag_2Se$ by Non-Stoichiometric Defects. *Appl. Phys. Lett.* **2022**, *120* (19), 193902.
(78) Wang, H.; Liu, X.; Zhou, Z.; Wu, H.; Chen, Y.; Zhang, B.; Wang, G.; Zhou, X.; Han, G. Constructing N-Type $Ag_2Se$/CNTs Composites toward Synergistically Enhanced Thermoelectric and Mechanical Performance. *Acta Mater.* **2022**, *223*, 117502.
(79) Lee, C.; Park, Y.-H.; Hashimoto, H. Effect of Nonstoichiometry on the Thermoelectric Properties of a $Ag_2Se$ Alloy Prepared by a Mechanical Alloying Process. *J. Appl. Phys.* **2007**, *101* (2), 24920.
(80) Han, S.; Wu, M.; Yuan, Z.; Ye, H.; Li, R.; Ge, B.; Zhou, C. Design Charged Edge Dislocations Toward High Performance Thermoelectrics. *Adv. Funct. Mater.* **2026**, *36* (36), e32103.
(81) Perez-Taborda, J. A.; Caballero-Calero, O.; Vera-Londono, L.; Briones, F.; Martin-Gonzalez, M. High Thermoelectric ZT in N–Type Silver Selenide Films at Room Temperature. *Adv. Energy Mater.* **2018**, *8* (8), 1702024.
(82) Li, D.; Zhang, B. L.; Ming, H. W.; Wang, L.; Zu, Y.; Qin, X. Y. Liquid-Phase Manipulation Securing Enhanced Thermoelectric Performance of $Ag_2Se$. *ACS Appl. Mater. Interfaces* **2021**, *13* (29), 34543–34549.
(83) Nan, B.; Li, M.; Zhang, Y.; Xiao, K.; Lim, K. H.; Chang, C.; Han, X.; Zuo, Y.; Li, J.; Arbiol, J.; Llorca, J.; Ibáñez, M.; Cabot, A. Engineering of Thermoelectric Composites Based on Silver Selenide in Aqueous Solution and Ambient Temperature. *ACS Appl. Electron. Mater.* **2024**, *6* (5), 2807–2815.
(84) Liao, Y.-Y.; Sun, Q.; Jiang, X.-P.; Wu, H.; Tian, B.-Z.; Wang, Z.-G.; Zheng, K.; Yang, L. Constructing Cell-Membrane-Mimic Grain Boundaries for High-Performance n-Type $Ag_2Se$ Using High-Dielectric-Constant $TiO_2$. *J. Mater. Sci. Technol.* **2024**, *179*, 138–144.
(85) Abdellaoui, L.; Chen, Z.; Yu, Y.; Luo, T.; Hanus, R.; Schwarz, T.; Bueno Villoro, R.; Cojocaru-Mirédin, O.; Snyder, G. J.; Raabe, D.; Pei, Y.; Scheu, C.; Zhang, S. Parallel Dislocation Networks and Cottrell Atmospheres Reduce Thermal Conductivity of PbTe Thermoelectrics. *Adv. Funct. Mater.* **2021**, *31* (20), 2101214.
(86) Wang, H.; Han, G.; Zhang, B.; Chen, Y.; Liu, X.; Zhang, K.; Lu, X.; Wang, G.; Zhou, X. $AgSbSe_2$ Inclusions Enabling High Thermoelectric and Mechanical Performance in N-Type $Ag_2Se$-Based Composites. *Acta Mater.* **2023**, *248*, 118753.
(87) Li, D.; Zhang, J. H.; Li, J. M.; Zhang, J.; Qin, X. Y. High Thermoelectric Performance for an $Ag_2Se$-Based Material Prepared by a Wet Chemical Method. *Mater. Chem. Front.* **2020**, *4* (3), 875–880.
(88) Chen, J.; Yuan, H.; Zhu, Y.-K.; Zheng, K.; Ge, Z.-H.; Tang, J.; Zhou, D.; Yang, L.; Chen, Z.-G. Ternary $Ag_2Se_{1-x}Te_x$: A Near-Room-Temperature Thermoelectric Material with a Potentially High Figure of Merit. *Inorg. Chem.* **2021**, *60* (18), 14165–14173.
(89) Qin, B.; He, W.; Zhao, L.-D. Estimation of the Potential Performance in P-Type SnSe Crystals through Evaluating Weighted Mobility and Effective Mass. *J. Mater.* **2020**, *6* (4), 671–676.
(90) Li, M.; Liu, Y.; Zhang, Y.; Han, X.; Xiao, K.; Nabahat, M.; Arbiol, J.; Llorca, J.; Ibañez, M.; Cabot, A. PbS–Pb–$Cu_xS$ Composites for Thermoelectric Application. *ACS Appl. Mater. Interfaces* **2021**, *13* (43), 51373–51382.
(91) Ciancio, R.; Dunin-Borkowski, R. E.; Snoeck, E.; Kociak, M.; Holmestad, R.; Verbeeck, J.; Kirkland, A. I.; Kothleitner, G.; Arbiol, J. E-DREAM: The European Distributed Research Infrastructure for Advanced Electron Microscopy. *Microsc. Microanal.* **2022**, *28* (S1), 2900–2902.





https://doi.org/10.1021/acsenergylett.6c01499
*ACS Energy Lett.* 2026, 11, 5752–5762